Fabrication and measurement of a photonic crystal waveguide integrated with a semiconductor optical amplifier

T. Cao,[1] Y.-L. D. Ho,[1] P. J. Heard,[1] L. P. Barry,[2] A. E. Kelly,[3] and M. J. Cryan[1,*]

[1]*Department of Electronic and Electrical Engineering, Centre for Communications Research, University of Bristol, Bristol, BS8 1UB, UK*
[2]*School of Electronic Engineering, Dublin City University, Dublin 9, Ireland*
[3]*Department of Electronics and Electrical Engineering, University of Glasgow, G12 8LT UK*
**Corresponding author: m.cryan@bristol.ac.uk*

Received July 10, 2008; revised November 30, 2008; accepted February 1, 2009;
posted February 19, 2009 (Doc. ID 98381); published March 23, 2009

A III-V semiconductor photonic crystal (PhC) waveguide is integrated into a semiconductor optical amplifier (SOA); this has the potential to reshape pulses that are distorted and chirped on propagation through the SOA. The PhC waveguide is modeled using the three-dimensional (3D) finite difference time domain (FDTD) method initially for the ideal case of infinite depth holes, and this shows a ministop band close to 1600 nm. The PhC waveguide is then fabricated into a commercial SOA using focused ion beam etching. The optical power measured at the output of the PhC-SOA waveguide shows evidence of a ministop band but with a small stopband depth. More realistic 3D FDTD modeling including effects of finite hole depth and vertical layer structure is then shown to give much better agreement with measured results. Finally predictions are made for the performance of a membrane structure. © 2009 Optical Society of America

OCIS codes: 130.3120, 130.5296.

1. INTRODUCTION

A photonic crystal (PhC) is a novel class of artificial material in which the propagation of light is controlled using a strong periodic modulation of the refractive index [1]. In the last decade, a large variety of unique functionalities for PhCs have been reported, such as low-loss guiding, slow light, and large group velocity dispersion (GVD) [2–7]. The light confinement and control offered by PhCs can be used to enhance the performance and reduce the size of many important optical components, such as lasers, semiconductor optical amplifiers (SOAs), and switches. In particular, PhC waveguides possessing ministop bands (MSBs), caused by mode coupling, have a number of interesting applications [8,9]. It has been shown that MSBs can perform pulse compression for both linear [10] and nonlinear chirped pulses [11]. In [12] it is shown that the negative group delay or fast-light phenomenon that occurs within the MSB is the major contributor to the pulse compression effect. Previous modeling work [11] has shown that there is potential for dispersion compensators to be integrated at the output of an SOA or laser to correct for, or even predistort, chirped output pulses.

This paper presents results for what is believed to be the first attempt to postprocess a PhC waveguide into a commercial SOA. SOAs and PhCs have been combined before using more conventional wafer scale processing [13,14]. The devices used in this paper are commercial grade SOAs and have been supplied by Dublin City University and are from Amphotonix Ltd. The PhC waveguide is designed to work near to the optical communication wavelength of 1550 nm and has been fabricated using focused ion beam (FIB) processing, prior to wafer scale electron beam processing [15–19]. FIB processing is a rapid and maskless nanofabrication technique that has been widely used in optics and optoelectronics to create device prototypes. Some advantages of FIB processing that make it unique for micro and nanofabrication are real-time imaging of the sample through secondary electron emission before, during, and immediately after etching and the accurate visual positioning of etch patterns on the samples. However, the high energy nature of FIB processing can sometimes cause damage to devices, but this can often be reduced or recovered using techniques such as gas assisted etching or annealing. In the work presented here a strong damage process is occurring within the etched PhC region such that after a number of hours the PhC pattern is no longer present. At this stage it is unclear whether this is related to oxidization or thermal processes; however, there is sufficient time to carry out a postetch measurement and interesting results have been observed. Potential passivation schemes are being investigated, but it is felt that electron beam lithography of complete SOAs with an integrated PhC section would be the best route to follow.

The rest of the paper is organized as follows. In Section 2 the PhC waveguide with an MSB near 1550 nm is modeled using the three-dimensional (3D) finite difference time domain (FDTD) method in the ideal case of infinite depth holes. In Section 3, an FIB fabrication process for the PhC-SOA is introduced and shows that a PhC can be fabricated, albeit with limited lifetime. In Section 4, SOA

 © 2009 Optical Society of America

transmission measurement results are shown at different temperatures and injection currents for each step of the fabrication process. In Section 5 further 3D FDTD modeling is carried out on more realistic device structures, and finally the performance of a membrane PhC waveguide is predicted.

2. THREE-DIMENSIONAL FDTD MODELING (I)

The modeling procedure uses modal FDTD [12]; here the fundamental TE mode of the SOA waveguide structure is launched into the FDTD simulation and overlap integrals can be performed with respect to this mode, which give accurate magnitude and phase responses. A full 3D simulation is carried out; Fig. 1(a) shows the top view of the structure and Fig. 1(b) shows a schematic cross section of the structure. The structure investigated here is a simplified version of that which will be fabricated and modeled later in the paper. This is a useful starting point for modeling since it is very idealized with "infinite" depth holes. The holes are shown passing vertically through the whole structure, and thus as far as the mode in the waveguide is concerned they are essentially "infinitely" deep. It should also be pointed out that this structure could be fabricated directly by more conventional electronic beam lithography techniques [13] that can achieve deep vertical holes but which require wafer scale processing. However, using FIB techniques some modifications to the structure are required but with the advantage that processing is very rapid and is done on a chip-by-chip basis. This structure is also straightforward to model in two-dimensions (2D) using the effective index method, and as will be seen later in this section this allows useful results to be obtained. To reduce the simulation RAM and run time requirements, the fact that the structure is symmetrical can be used to reduce the problem size. It is well known that if is a structure is symmetrical and is excited by a symmetrical mode then all the solutions must be symmetrical. This enables a perfect electric conducting (PEC) boundary to be placed at the center of the waveguide and only the lower half of the structure to be simulated without altering the results. This is only true for TE mode excitation; for TM mode excitation a perfect magnetic boundary would be required. The light propagates along the Γ-K direction and the PhC has a lattice constant $a=480$ nm and a radius $r=158$ nm. The vertical spacing between rows has been adjusted slightly from 416 to 420 nm in order to match the FDTD grid. In this case the width of the waveguide has been increased from W_3 (1.66 μm) to $W_{3.6}$ (2 μm) in order to obtain an MSB in the region of 1550 nm [20,21].

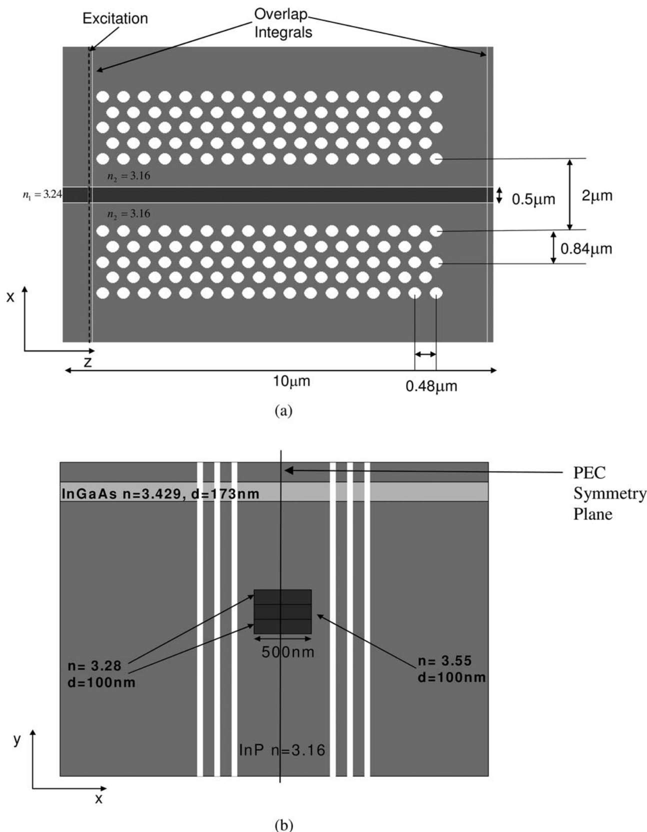

Fig. 1. (a) Top view of SOA-PhC waveguide with $a=480$ nm, $r/a=0.329$, Γ-K direction, and total model length=10 μm (PhC waveguide length is 17 holes long, 7.68 μm center-to-center). Only bottom half of structure is simulated due to symmetry. (b) Schematic cross section of SOA-PhC waveguide with infinite depth holes showing thickness d of active region layers and refractive index values used. Also shows a perfect electric conductor (PEC) symmetry plane.

Dimensions and refractive indices of the active region have been approximated from more detailed data from Amphotonix. The waveguide is tapered as it approaches the facet from 1.4 to 0.4 μm for mode matching purposes. Since the PhC waveguide is much shorter than the length of the taper, the effect of tapering has not been included and a width of 500 nm has been chosen.

Variable meshing is used with minimum mesh sizes of $\Delta x=19.23$ nm, $\Delta y=20$ nm, and $\Delta z=20$ nm; this results in a run time of around 1.5 on a Pentium 4 and requires 800 MB of RAM. The waveguide is excited by the fundamental TE mode at the input of the structure shown by the dashed line in Fig. 1 and 2 shows the spatial distribu-

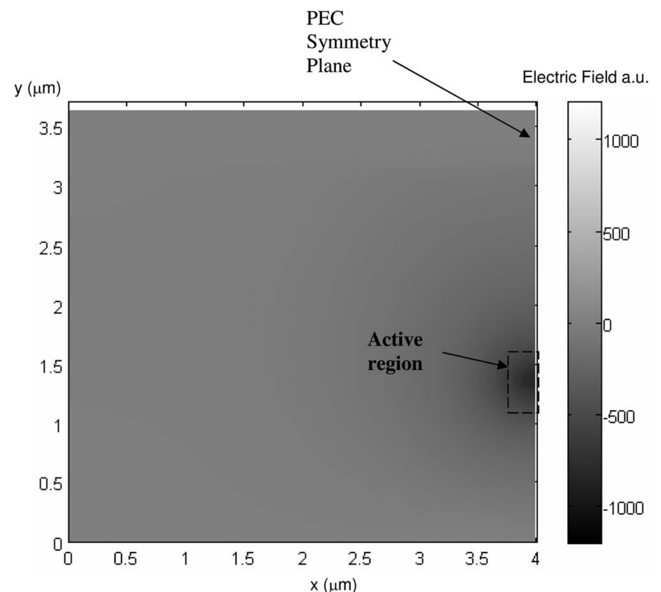

Fig. 2. Spatial distribution of Re(E_x) for the fundamental mode across the waveguide in Fig. 1(b).

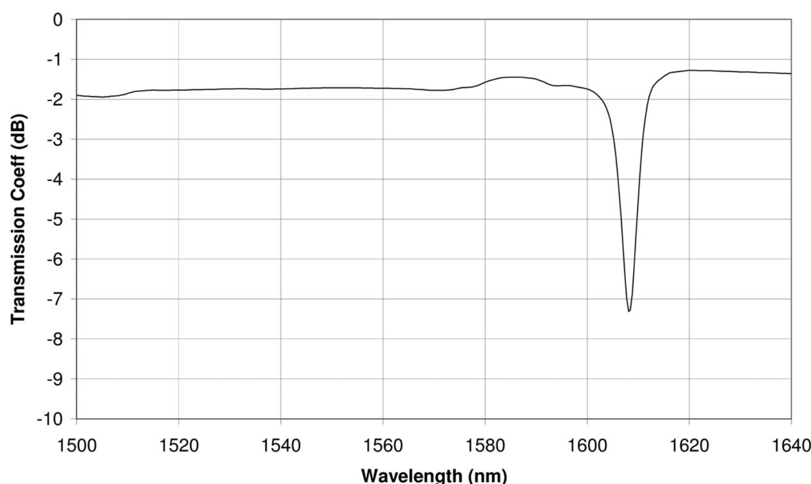

Fig. 3. FDTD simulated transmission for waveguide of Fig. 1.

tion of the real part of E_x for the mode in a straight non-PhC waveguide. The transmission response of the structure is calculated by first performing a simulation with a simple straight waveguide and no PhC present in order to remove the effects of reflection from the PhC waveguide. The input intensity is calculated by taking an overlap integral with respect to the fundamental mode at the input. A fast fourier transform (FFT) is performed on these data to convert to the frequency domain. This procedure is repeated at the output of the guide with the PhC waveguide present. The ratio of these two intensities gives the transmission coefficient.

Figure 3 shows the FDTD transmission response, and the MSB is clearly observed near 1610 nm. Since this is a 3D calculation out-of-plane losses will be occurring, and this accounts for the general level of "background" loss of around 1.5 dB and the limited depth of the MSB. The background loss will be caused by scattering at the transition from the SOA waveguide to the PhC-SOA waveguide. This could be improved by tapering the input and the output of the PhC waveguide. The MSB can be made deeper by increasing the length of the device and increasing the number of rows of holes in the sidewalls. To confirm that this is indeed an MSB a 2D plane wave expansion calculation is performed using MPB [22]. For this calculation we have used the effective index method to reduce the 3D structure to 2D, and we have used a 1D mode solver to determine the effective refractive index of the central active region. We have used a value of $n=3.24$ for the active region and $n=3.16$ for the nonactive regions. The results are shown in Fig. 4, and it can be seen that the MSB occurs at $a/\lambda=0.2985$, which gives $\lambda=1608$ nm for a lattice constant of 480 nm. This is very close to the 3D FDTD results, and the slight difference is caused by the inaccuracies inherent in the effective index approximation.

MSBs are particularly sensitive to sidewall thickness due to the fact that they rely on higher order modes that tend to be much more extended than the fundamental mode. Section 5 will show in more detail how the depth of

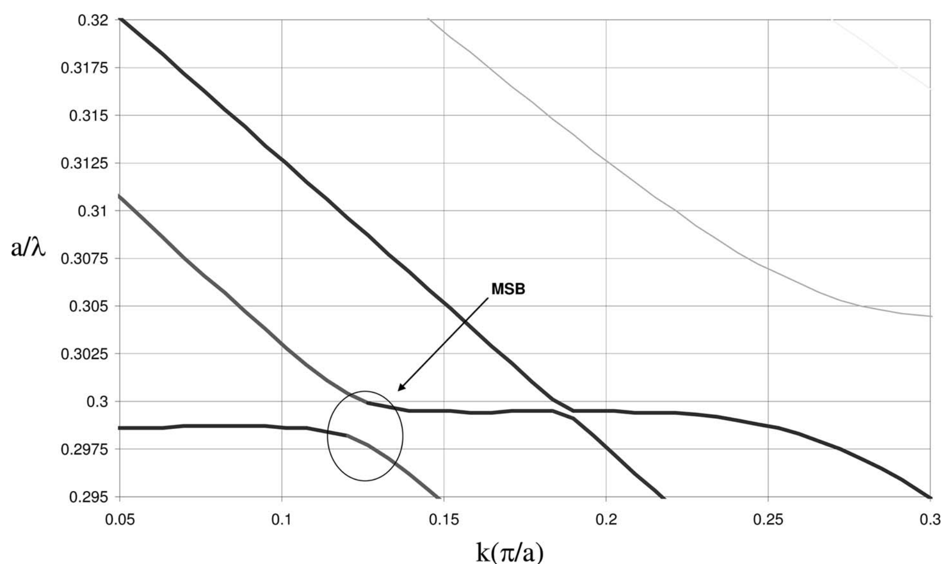

Fig. 4. Dispersion diagram for waveguide of Fig. 1(a) simulated by MPB showing position of the MSB.

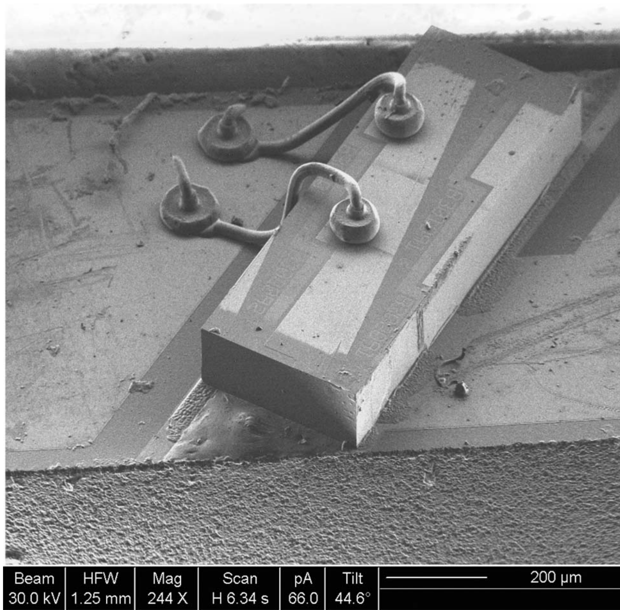

Fig. 5. Top view of the SOA without trench. The SOA chip is bonded to an aluminium nitride submount and wire bonded to enable electrical injection.

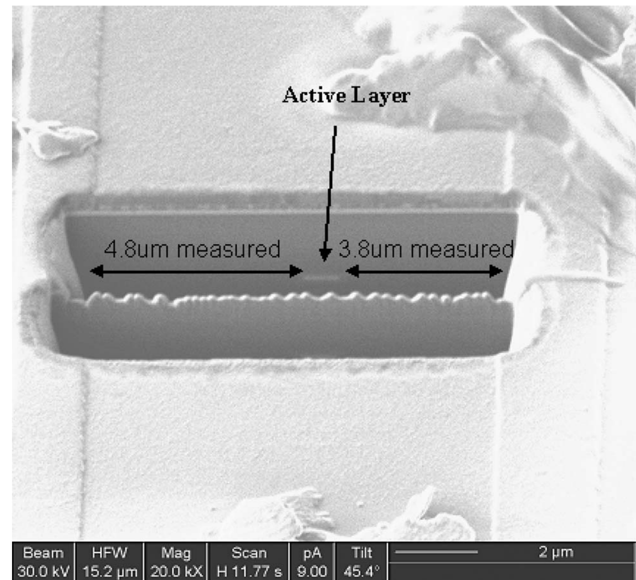

Fig. 6. Cross section of the SOA showing distance from active region to edge of ridge (FIB image).

the MSB can be controlled. Having obtained an MSB within the operating band of the SOA, FIB processing is now used to implement this within the device.

3. FABRICATION

The SOAs being used are commercial grade devices that have been fully characterized prior to shipping and are mounted and wire bonded to an aluminium nitride submount. Figure 5 shows an FIB image of the device prior to processing.

The SOAs are angled facet devices with a buried InP-InGaAsP heterostructure active region. This makes them ideally suited to FIB processing since the beam does not have to directly etch through the active region. A FIB cross section of the SOA, which is shown in Fig. 6, can be used to find the accurate position of the active region and thus as a reference to align the holes on both sides of the channel. A two stage etching procedure is then carried out; this is required because when doing direct FIB etching, sidewall verticality can be difficult to maintain for very deep holes. Thus material is removed from above the active region—termed a trench etch—such that 1 μm deep holes, which are achievable using FIB, can be etched, which will overlap a large proportion of the optical mode.

Figure 7 shows a schematic cross section of the trench etch with a depth of 2.3 μm, which produces a very flat surface that is 200 nm above the active region. The device is rotated through 90° in order to perform this etch and the current used is 350 pA. Figure 8 shows the FIB image of the SOA after etching the trench; it is seen that a very smooth flat area is achieved in preparation for etching the PhC.

Having created a flat surface approximately 200 nm above the active layer the PhC waveguide can now be etched into the device. The structure is etched into the SOA using a low beam current of 11 pA. Figures 9 shows a 3D view of the structure. Due to a mask generation error, the fabricated structure is slightly longer than the modeled one at 19 holes (8.64 μm center-to-center) rather than 17 holes (7.68 μm center-to-center) as in Fig. 1(a). This will only have a minor effect on the results since adding a further two rows of holes will create a very slightly

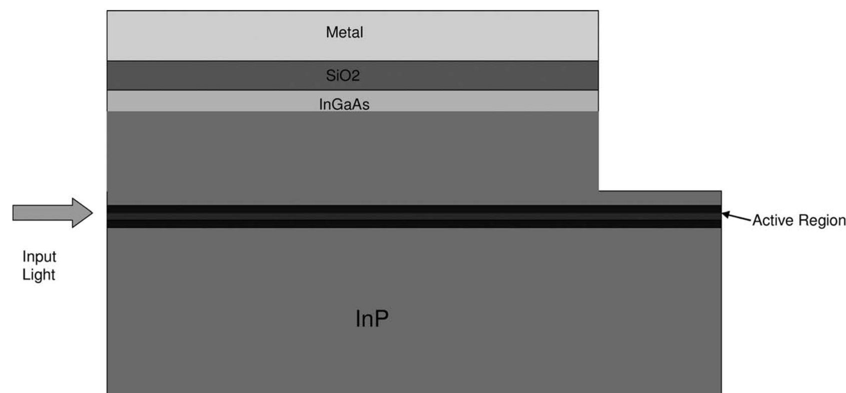

Fig. 7. Schematic cross sectional view of the SOA with integrated trench at the output.

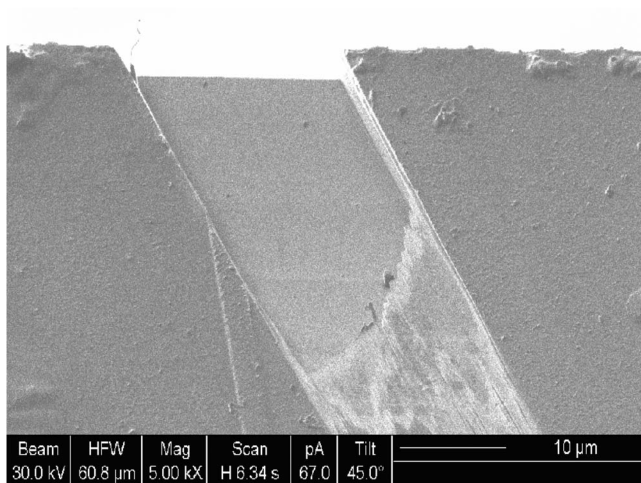

Fig. 8. Top view of the SOA integrated with the trench.

deeper MSB but will have little effect on the MSB position or bandwidth as seen in the detailed study of length effects in [12].

A critical part of the PhC etching process is placing the PhC waveguide symmetrically about the active region, and a procedure has been developed for this. First, a cross section of the SOA is done, as shown in Fig. 6, in a test sample to find the accurate position of the buried heterostructure. Then the distance from the active region to the edge of the ridge can be measured as shown. A new SOA device is then mounted and an alignment mark is placed 3.8 μm away from the right side of the ridge by using a 9 pA beam to show the position of the active region. The alignment accuracy is estimated to be ±50 nm for this procedure. The final etched device showing the alignment mark is shown in Fig. 10.

Figure 10 shows that a well defined set of holes have been etched. An 11 pA beam current is selected to drill the holes in order to maintain good hole profiles [16]. However the rows of holes closest to the active region must be etched very carefully such that they do not overlap with the active region in order to reduce damage to the quantum wells. In this paper, we designed the width of the line defect of the PhC waveguide to be 2 μm; future designs will be made with wider waveguide cores such that the tolerances of the alignment procedure can be relaxed. This will impact the spectral width and position of the MSB, and thus a reoptimization of the PhC waveguide in terms of lattice constant and r/a ratio will be required.

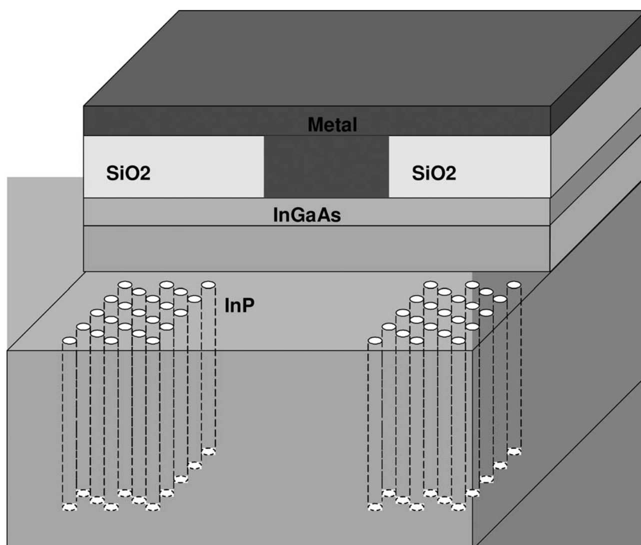

Fig. 9. Schematic 3D view of the SOA with integrated PhC waveguide at the output.

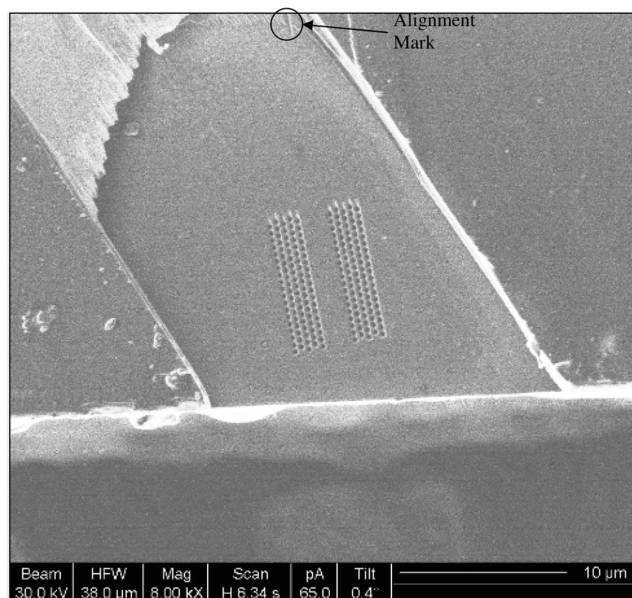

Fig. 10. Top view of the SOA with integrated PhC waveguide. The fabricated waveguide is slightly longer than the modeled one shown in Fig. 1(a) at 19 holes long (8.64 μm center-to-center). All other parameters are the same.

4. MEASUREMENT

A schematic of the measurement setup is shown in Fig. 11. A tunable laser source is used to measure the transmission response of the device. Prior to etching, the devices have been measured using a cleaved facet single mode fiber (SMF) to couple light into and out of the device. Ideally these would be lensed fibers, however, these were unavailable at the time of measurement; this results in poor coupling efficiency and thus low gain for the de-

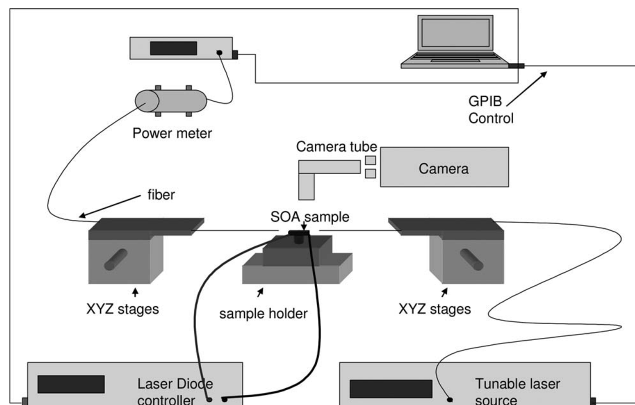

Fig. 11. Schematic of the measurement setup.

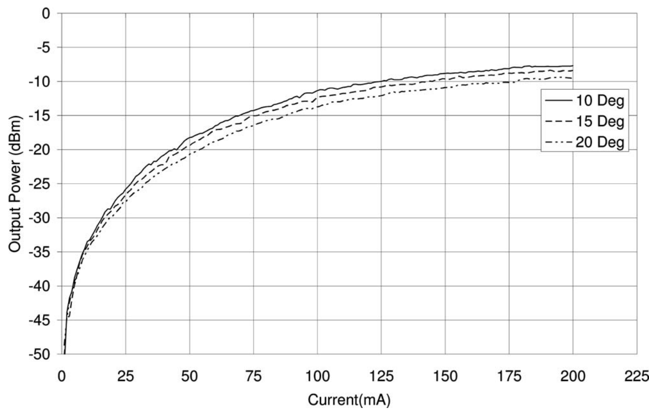

Fig. 12. $L-I$ curve of the SOA before FIB etching at 10°C, 20°C, and 30°C.

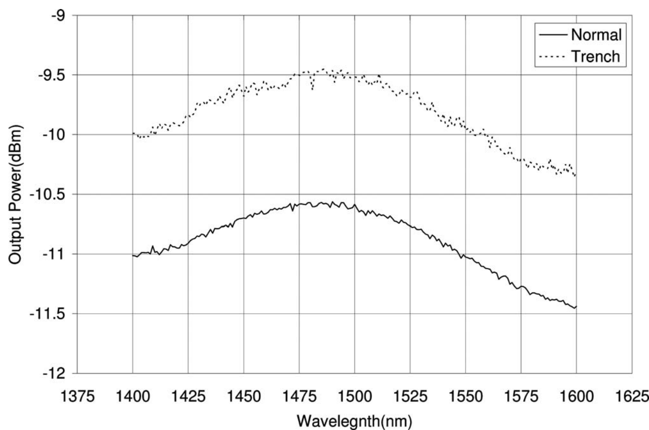

Fig. 13. Output power from the SOA with and without trench at the output, where $T_{\mathrm{mount}}=20°\mathrm{C}$ and $I=200$ mA.

vices. The output power is read by the power meter. A laser diode controller is used to inject current into the sample and in combination with a Peltier cooler keeps the working temperature as required. The measurement is performed by computer control by connecting the tunable laser, power meter, and temperature controller to the desktop via general-purpose interface bus (GPIB). The temperature dependence of the $L-I$ curve of an unetched device is measured and shown in Fig. 12 in the range of 10°C–20°C with $P_{\mathrm{in}}=-10$ dBm. These curves show the expected trend of reducing gain at a higher temperature [23].

The output power as a function of wavelength was then measured and is shown in Fig. 13 with $I=200$ mA, $T=20°\mathrm{C}$, and $P_{\mathrm{in}}=-10$ dBm. It can be seen that no gain is being obtained due to a poor coupling efficiency. However, in this paper, relative performance before and after etching is the main criterion. The output power of the device was then re-measured after etching the trench and is also shown in Fig. 13. It can be seen that in fact better performance is being obtained now, but there will be 1–2 dB repeatability in these types of measurements due to fiber alignment. The main point to observe is that no major degradation in performance has occurred.

After drilling the holes into the output of SOA, the device is then remeasured and the results are shown in Fig. 14. It can be seen that a distinct “dip” is observed around 1539 nm, and it is believed that this is an MSB feature. This measured feature is different from the one shown in Section 2. This is due to a number of factors as will be discussed later in Section 5.

Tunability of such a notch feature would be very useful, and tuning of semiconductor optoelectronic devices [23,24] and PhCs [25–28] has been investigated by a number of workers. To this end measurements have been taken at two different current levels both with $T=20°\mathrm{C}$ and $P_{\mathrm{in}}=-10$ dBm. Figure 14 shows that the notch wavelength can be tuned over 2 nm for a 100 mA change in bias current. The tuning mechanism here is likely to be a carrier induced refractive index change, and this has been widely used and studied as a tuning mechanism in semiconductor devices [24]. Another widely used mechanism is temperature tuning [25] and evidence of such tuning has been observed in Fig. 15. The amount of tuning observed is consistent with 0.1 nm/C as shown in [25]. Future work will attempt to optimize the amount of tuning achievable.

Unfortunately the MSB feature has a limited lifetime

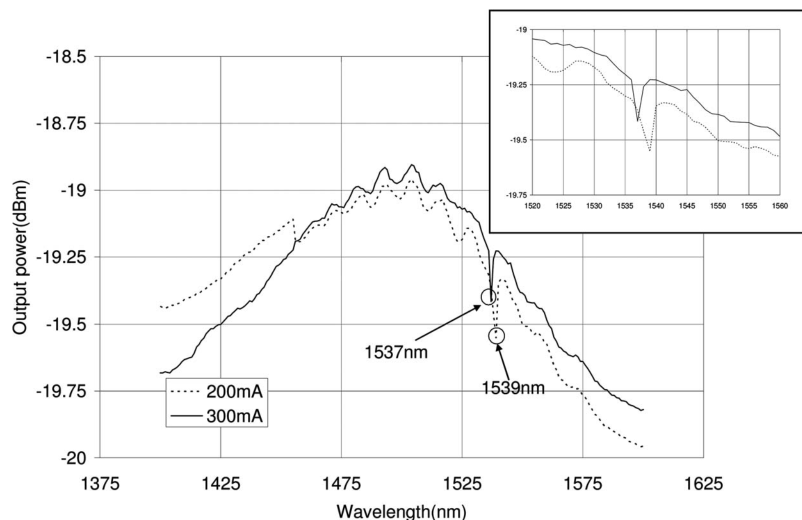

Fig. 14. Output power from the SOA with PhC waveguide at two different bias currents and $T_{\mathrm{mount}}=20°\mathrm{C}$. Inset shows details of resonances.

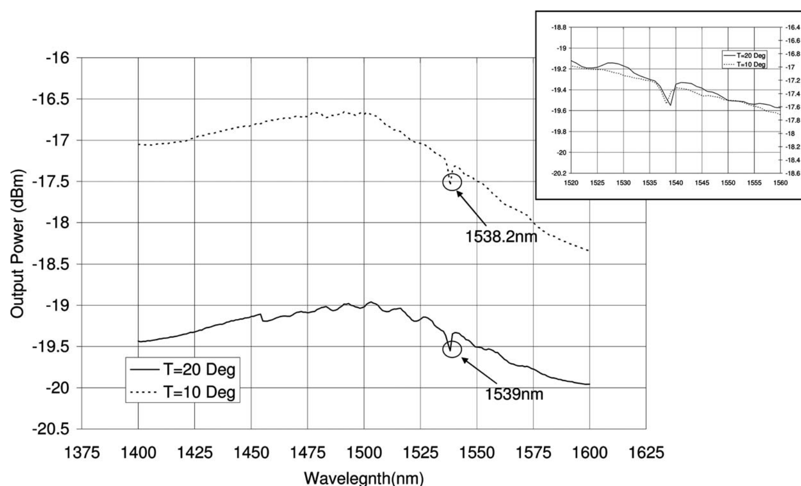

Fig. 15. Output power from the SOA with PhC waveguide at two different temperature $T_{\text{mount}}=10°\text{C}$, $20°\text{C}$ with the same bias current 200 mA. The inset shows a zoom in on data and uses two y-axes; left hand axis is 20°, right hand axis is 10°.

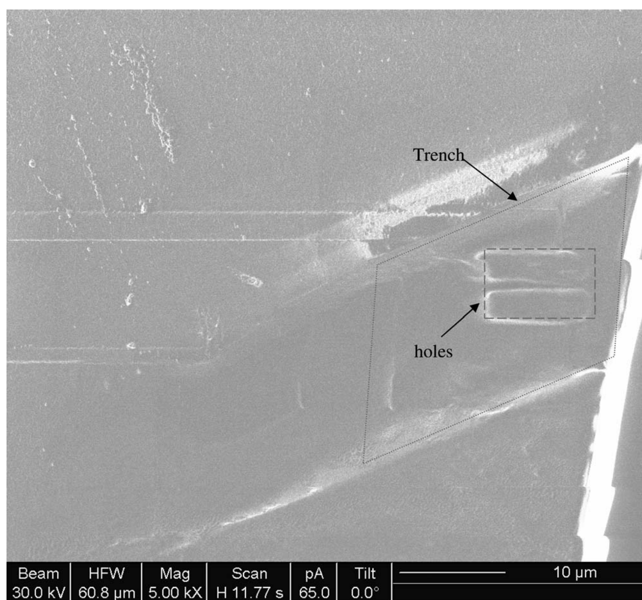

Fig. 16. FIB image of the PhC waveguide after exposure to air for approximately 10 h.

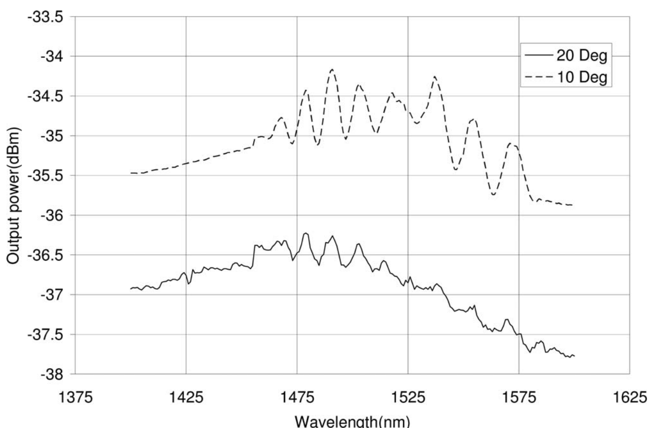

Fig. 17. Measurement of the output power of the device after damage effect to holes of PhC.

in that after around 10 h the notch feature disappears and further inspection of the device as shown in Fig. 16 shows that the holes defining the PhC waveguide are no longer present. The device has been remeasured and the output power is shown in Fig. 17; it can be seen that much lower output power is now being obtained. It is not clear at this stage what is causing this damage, but it may be a type of oxidization or thermal effect that is damaging the hole structure and then when viewed in the FIB the beam is removing the damaged material and hence the holes. It may be possible to use a passivation procedure to reduce the damage, but wafer scale E-beam processing, which is now well established in material systems such as this, would suffer much less from these types of damage effects.

5. THREE-DIMENSIONAL FDTD MODELING (II)

The measured results in Section 4 have shown evidence of an MSB feature. The main discrepancy with the initial 3D modeling results is that the depth of the notch is orders of

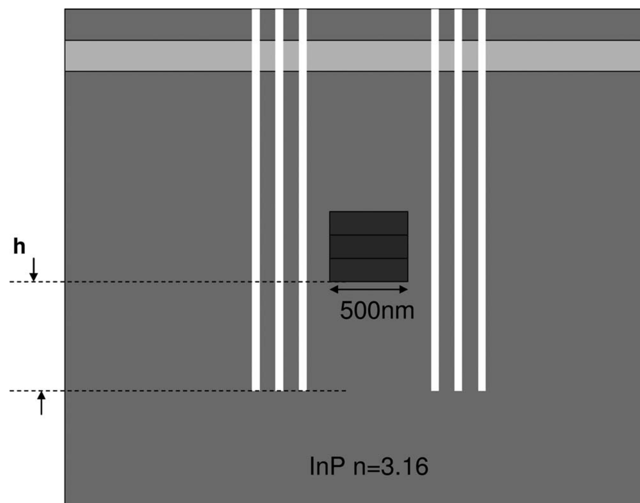

Fig. 18. Cross section of 3D FDTD model with finite depth hole showing a depth relative to the bottom of active region.

magnitude less in the measured case. There is also a wavelength shift in the measured results. This section seeks to improve the agreement by using a more realistic model for the device. The first feature to be introduced is finite hole depth as shown in Fig. 18.

It is believed that the holes are etched approximately 1 μm below the surface of the trench. Thus the depth has been reduced and two different depths 1 μm ($h=500$ nm) and 1.158 μm ($h=658$ nm) have been modeled. The results are shown in Fig. 19. It can be seen that the MSB has reduced in depth from approximately 5 to 2–3 dB. This reduction is caused by light leaking out beneath the holes as a consequence of the large mode size due to the relatively weak confinement in the active region; such effects have been studied in detail by a number of workers [29,30]. It can also be seen that there is approximately a 0.6 dB reduction in depth of MSB when going from $h=0.658$ to 500 nm.

The next important feature added to the model is the effect of the air trench that has been shown in Fig. 9. This brings air to within 200 nm of the active region and thus will have a large impact on the guided modes. Figure 20 shows the modeled results for this case.

These results show two effects; first the depth of the MSB is further reduced to 0.7 dB for $h=658$ nm and 0.5 dB for $h=500$ nm, and the wavelength has shifted to the region of 1580 nm. The reduction in depth is caused by the presence of the air trench shifting the mode further down into the structure resulting in more leakage of light beneath the holes. This is confirmed when full depth holes are modeled and the depth of the MSB returns to almost the same level as in Fig. 3. The shift down in wavelength is mainly caused by the presence of air reducing the effective index of the structure producing a reduction in the MSB wavelength. The position of the anticrossing in the band structure that produces the MSB will also be sensitive to the geometry of the holes, hence the shift in wavelength between $h=658$ and 500 nm. There is a further feature that the general background loss has increased to 4 dB. This is due partly to the fact that there will be more scattering loss in the transition from the SOA waveguide to the air trench PhC waveguide. However, part of this loss is also numerical due to the fact that the air trench extends to the end of the waveguide into the region where the overlap integrals are calculated. These overlaps refer to the fundamental mode of the SOA waveguide, and the air trench will therefore introduce an inaccuracy here. The alternative is to not the let the air trench go into the overlap calculation region, however, this will result in a scattering loss of a second transition and Fabry–Perot oscillations that are not occurring in the real device. The solution to this is to allow overlaps between arbitrary modes to be calculated; it is hoped to implement this in our code in the near future.

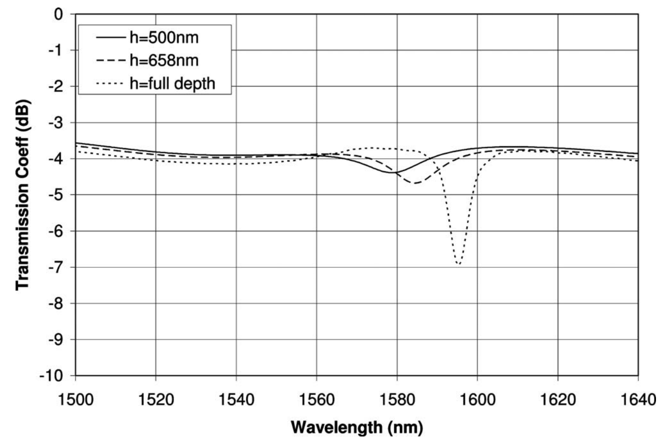

Fig. 20. 3D FDTD model of transmission through PhC waveguide with an air trench 200 nm above active region and different depth holes, $h=500$ and 658 nm and full depth.

These results are now much closer to the measured ones, and the further reduction in depth of the MSB could be due to the holes being slightly shallower than 1 μm and the trench being closer than 200 nm to the active region. A slightly deeper trench will also shift the MSB wavelength closer to the measured one. Also it should be noted that lossless dielectrics have been used in this model; in reality there will be material losses that will affect the MSB depth. The fact that the measured device is 19 holes long rather than 17 will only have a very minor effect on the depth and the position of the MSB [12].

The modeling has shown that the fabrication approach here leads to a much reduced MSB depth and much deeper holes would be needed to obtain the results as shown in Fig. 4. These depths—around 3–4 μm deep—have been achieved for GaAs and InP based PhC devices

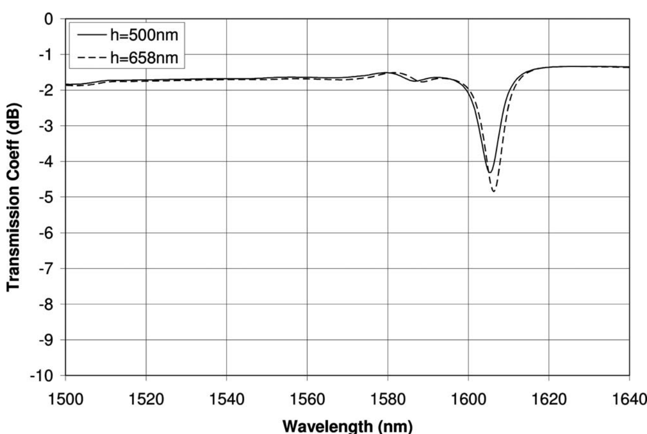

Fig. 19. 3D FDTD model of transmission through PhC waveguide with finite depth holes for $h=500$ and 658 nm.

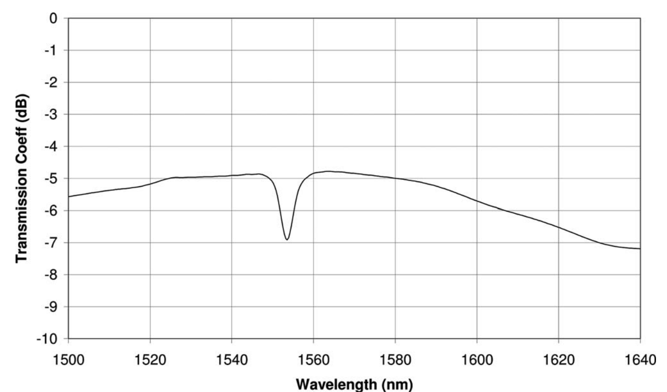

Fig. 21. 3D FDTD model of transmission through PhC waveguide with finite depth, $h=658$ nm holes and air trench 200 nm above and below the active region.

using *E*-beam processing. An alternative route is to consider a membrane structure, where an air undercut is introduced into the structure beneath the active region. This can also be fabricated using the FIB or *E*-beam processing using sacrificial layers. The 3D model can be used to predict the performance of such a device. To this end an air undercut was introduced 200 nm below the active region; the results for this are shown in Fig. 21.

Figure 21 shows that the strong vertical confinement recovers some of the MSB depth; however the scattering loss at the transition is slightly higher now at around 5 dB. Tapering will help this to some extent, but it is hoped that the gain available in the SOA will be sufficient to offset these losses.

6. CONCLUSIONS

This paper has presented the integration of a PhC waveguide into an SOA. The 3D FDTD method has been used to design an MSB close to 1600 nm, and this has been shown previously to enable pulse reshaping and compression to be performed. The PhC waveguide is realized by means of FIB etching, which can achieve 1 μm deep holes with a reasonable hole profile. Experimental data are obtained and the results suggest the existence of an MSB feature; 3D FDTD is then used to include more realistic device features, such as finite hole depth and the air trench etch, and this shows much better agreement with measured results than initial modeling. The 3D modeling highlights the problem of out-of-plane losses in weak vertically confined systems and modeling of a membrane structure shows that a reasonable MSB can be obtained for this case. In terms of fabrication, annealing and passivation will be investigated in the future to recover the damage induced by the FIB etching.

ACKNOWLEDGMENTS

This work was funded by the Ultrafast Photonics Collaboration (UPC), UK (www.ultrafast-photonics.org). The authors would like to thank Joe McGeehan for the use of the Condor computing cluster that was donated to Bristol EE by Toshiba Research Labs Europe. They would also like to thank Phil Wade and Patrick Townsend who implemented and maintained the cluster.

REFERENCES

1. E. Yablonovitch, “Inhibited spontaneous emission in solid-state physics and electronics,” Phys. Rev. Lett. **58**, 2059–2062 (1987).
2. Y. A. Vlasov, M. O’Boyle, H. F. Hamann, and S. J. McNab, “Active control of slow light on a chip with photonic crystal waveguides,” Nature **438**, 65–69 (2005).
3. K. Inoue, and N. Kawai, Y. Sugimoto, N. Carlsson, N. Ikeda, and K. Asakawa, “Observation of small group velocity in two-dimensional AlGaAs-based photonic crystal slabs,” Phys. Rev. B **65**, 121308 (2002).
4. M. Notomi, K. Yamada, A. Shinya, J. Takahashi, C. Takahashi, and I. Yokohama, “Extremely large group-velocity dispersion of line-defect waveguides in photonic crystal slabs,” Phys. Rev. Lett. **87**, 253902 (2001).
5. V. Berger, “Nonlinear Photonic Crystals,” Phys. Rev. Lett. **81**, 4136–4139 (1998).
6. J. Li, T. P. White, L. O’Faolain, A. Gomez-Iglesias, and T. F. Krauss, “Systematic design of flat band slow light in photonic crystal waveguides,” Opt. Express **16**, 6227–6232 (2008).
7. S. Olivier, M. Rattier, H. Benisty, C. Weisbuch, C. J. M. Smith, R. M De La Rue, T. F. Krauss, U. Oesterle, and R. Houdre, “Mini-stopbands of a one-dimensional system: the channel waveguide in a two-dimensional photonic crystal,” Phys. Rev. B **63**, 113311 (2001).
8. T. Baba, N. Fukaya, and J. Yonekura, “Observation of light transmission in photonic crystal waveguides with bends,” Electron. Lett. **35**, 654–655 (1999).
9. T. J. Karle, Y. J. Chai, C. N. Morgan, I. H. White, and T. F. Krauss, “Observation of pulse compression in photonic crystal coupled cavity waveguides,” J. Lightwave Technol. **22**, 514–520 (2004).
10. T. Cao, M. J. Cryan, P. S. Ivanov, Y-L. D. Ho, G. B. Ren, I. J. Craddock, J. M. Rorison, and C. J. Railton, “Modelling of chirped pulse propagation through a MSB in a 2D PhC Waveguide,” J. Opt. Soc. Am. B **24**, 1575–1583 (2007).
11. T. Cao, M. J. Cryan, I. J. Craddock, J.-Z. Zhang, I. Galbraith, T. Karle, S. Yu, J. Rorison, and C. J. Railton, “Modelling of a 2D photonic crystal waveguide pulse reshaper integrated with a SOA,” in *Proceedings of CLEO* Munich, Germany, June 12–17, 2005.
12. T. Cao, M. J. Cryan, Y.-L. D Ho, I. J. Craddock, and C. J. Railton, “Fast-light based pulse compression in 2-D photonic crystal waveguides,” J. Lightwave Technol. **25**, 2590–2599 (2007).
13. E. Mizuta, H. Watanabe, and T. Baba, “All semiconductor low-Δ photonic crystal waveguide for semiconductor optical amplifier,” Jpn. J. Appl. Phys., Part 1 **45**, 6116–6120 (2006).
14. E. M Izuta and N. Yokouchi, “Characterization of photonic crystal waveguide for SOA operation,” in *Proceedings of Pacific Rim Conference Laser, and Electro-Optics* (2005), paper CThE1-4.
15. L. Giannuzzi and F. Stevie, *Introduction to Focused Ion Beams Instrumentation, Theory, Techniques, and Practices* (Springer, 2005).
16. M. J. Cryan, M. Hill, D. Cortaberria Sanz, P. J. Heard, L. Tian, S. Yu, and J. M. Rorison, “Focused ion beam based fabrication of nanostructured photonic devices,” IEEE J. Sel. Top. Quantum Electron. **11**, 1266–1278 (2005).
17. D. Freeman, C. Grillet, M. W. Lee, C. L. C. Smith, Y. Ruan, A. Rode, M. Krolikowska, S. Tomljenovic-Hanic, C. Martijn de Sterke, M. J. Steel, B. L. Davies, S. Madden, D. J. Moss, Y. H. Lee, and B. J. Eggleton, “Chalcogenide glass photonic crystals,” Photonics Nanostruct. Fundam. Appl. **6**, 3–11 (2008).
18. D. Freeman, S. Madden, and B. Luther-Davies, “Fabrication of planar photonic crystals in a chalcogenide glass using a focused ion beam,” Opt. Express **13**, 3079–3086 (2005).
19. G. Dale, R. M. Langford, P. J. S. Ewen, and C. M. Reeves, “Fabrication of photonic band gap structures in As40S60 by focused ion beam milling,” J. Non-Cryst. Solids **913**, 266–269 (2000).
20. M. J. Cryan, R. Varrazza, M. Cowin, M. Hill, I. J. Craddock, S. Yu, C. J. Railton, and J. M. Rorison, “Design, and simulation of a photonic crystal waveguide filter using the FDTD method,” in *Proceedings of LEOS*, Glasgow, UK, Nov. 5–16, 2002.
21. E. Viasnoff-Schwoob, C. Weisbuch, H. Benisty, C. Cuisin, E. Derouin, O. Drisse, G.-H. Duan, L. Legouézigou, F. Pommereau, S. Golka, H. Heidrich, H. J. Hensel, and K. Janiak, “Compact wavelength monitoring by lateral outcoupling in wedged photonic crystal multimode waveguides,” Appl. Phys. Lett. **86**, 101107 (2005).
22. S. G. Johnson and J. D. Joannopoulos, “Block-iterative frequency-domain methods for Maxwell’s equations in a planewave basis,” Opt. Express **8**, 173–190 (2001).
23. T. Kimura, S. Björlin, J. Piprek, and J. E. Bowers, “High-temperature characteristics and tunability of long-wavelength vertical-cavity semiconductor optical

amplifiers," IEEE Photon. Technol. Lett. **15**, 1501–1503 (2003).
24. B. R. Bennett, R. A. Soref, and J. A. Del Alamo, "Carrier-induced change in refractive GaAs and InGaAsP index of InP," IEEE J. Quantum Electron. **26**, 113–122 (1990).
25. B. Wild, R. Ferrini, R. Houdré, M. Mulot, S. An, and C. J. M. Smith, "Temperature tuning of the optical properties of planar photonic crystal microcavities," Appl. Phys. Lett. **84**, 846–848 (2004).
26. H. M. H. Chong and R. M. De La Rue, "Tuning of photonic crystal waveguide microcavity by thermooptic effect," IEEE Photon. Technol. Lett. **16**, 1528–1530 (2004).
27. S. W. Leonard, H. M. van Driel, J. Schilling, and R. B. Wehrspohn, "Ultrafast band-edge tuning of a two-dimensional silicon photonic crystal via free-carrier injection," Phys. Rev. B **66**, 161102 (2002).
28. J. Martz, R. Ferrini, F. Nüesch, L. Zuppiroli, B. Wild, L. A. Dunbar, R. Houdré, M. Mulot, and S. Anand, "Liquid crystal infiltration of InP-based planar photonic crystals," J. Appl. Phys. **99**, 103105 (2006).
29. H. Benisty, P. H. Lalanne, S. Olivier, M. Rattier, C. Weisbuch, C. J. M. Smith, T. F. Krauss, C. Jouanin, and D. Cassagne, "Finite-depth, and intrinsic losses in vertically etched two-dimensional photonic crystals," Opt. Quantum Electron. **34**, 205–215 (2002).
30. M. J. Cryan, I. J. Craddock, S. Yu, C. J. Railton, and J. M. Rorison, "Analysis of losses in 2D photonic crystal waveguides using the 3D finite difference time domain (FDTD) method," in *Proceedings of LEOS* Glasgow, UK, Nov. 10–14, 2002.